Degradation Mechanisms at the $Li_{10}GeP_2S_{12}$ / $LiCoO_2$ Cathode Interface in an All-Solid-State Lithium Ion Battery

Journal:	*ACS Applied Materials & Interfaces*
Manuscript ID	am-2018-05132c.R2
Manuscript Type:	Article
Date Submitted by the Author:	01-Jun-2018
Complete List of Authors:	Zhang, Wenbo; Physikalisch-Chemisches Institut, Justus-Liebig-Universität Gießen Richter, Felix; Justus-Liebig-University Giessen, Institute of Physical Chemistry Culver, Sean; Justus Liebig Universitat Giessen, Leichtweiß, Thomas; Physikalisch-Chemisches Institut, Justus Liebig Universität Gießen Lozano, Juan; University of Oxford, Dietrich, Christian; Justus-Liebig-University Giessen, Institute of Physical Chemistry Bruce, Peter; University of Oxford, Department of Materials Zeier, Wolfgang; Justus-Liebig-University Giessen, Institute of Physical Chemistry Janek, Jürgen; Justus-Liebig-Universitaet Giessen, Institute of Physical Chemistry

Degradation Mechanisms at the $Li_{10}GeP_2S_{12}$ / $LiCoO_2$ Cathode Interface in an All-Solid-State Lithium Ion Battery

Wenbo Zhang[a], Felix H. Richter[a,b], Sean P. Culver[a], Thomas Leichtweiss[a], Juan G. Lozano[b], Christian Dietrich[a], Peter G. Bruce[b], Wolfgang G. Zeier[a*], Jürgen Janek[a*]

[a] Physikalisch-Chemisches Institut & Center for Materials Research, Justus-Liebig-Universität Giessen, Heinrich-Buff-Ring 17, 35392 Giessen, Germany

[b] Departments of Materials and Chemistry, University of Oxford, OX1 3PH, Oxford, United Kingdom

Abstract

All-solid-state batteries (ASSBs) show great potential for providing high power and energy density with enhanced battery safety. While new solid electrolytes (SEs) have been developed with high enough ionic conductivities, SSBs with long operational life are still rarely reported. Therefore, on the way to high performance and long-life ASSBs, a better understanding of the complex degradation mechanisms, occurring at the electrode / electrolyte interfaces is pivotal. While the lithium metal / solid electrolyte interface is receiving considerable attention due to the quest for high energy density, the interface between the active material and solid electrolyte particles within the composite cathode is arguably the most difficult to solve and to study. In this work, multiple characterization methods are combined to better understand the processes that occur at the $LiCoO_2$ cathode and the $Li_{10}GeP_2S_{12}$ solid electrolyte interface. Indium and $Li_4Ti_5O_{12}$ are used as anode materials to avoid the instability problems associated with Li metal anodes. Capacity fading and increased impedances are observed during long-term cycling. Post-mortem analysis with scanning transmission electron microscopy (STEM), electron energy loss spectroscopy (EELS), x-ray diffraction (XRD) and x-ray photoelectron spectroscopy (XPS) show that electrochemically driven mechanical failure and degradation at the cathode / solid electrolyte interface contribute to the increase in internal resistance and the resulting capacity fading. These results suggest that the development of electrochemically more stable SEs and the engineering of cathode / SE interfaces are crucial for achieving reliable SSB performance.

Keywords: solid-state battery, $Li_{10}GeP_2S_{12}$, interface, XPS, degradation, solid electrolyte

Introduction

The growing need for reliable electric transportation options has imposed more demanding requirements on battery systems, specifically on the aspects of stability, safety and power / energy density. In the past 30 years, the conventional Li-ion battery (LIB), with organic liquids as electrolytes, has been developed and applied in almost all storage technologies.[1,2] However, further improvement is inter alia restricted by the intrinsic drawbacks of the organic liquid electrolytes (LEs). Thermal instability and flammability of LEs are threats to battery safety. Furthermore, the dissolution of metal ions from cathode active materials (CAM) into LEs triggers "chemical-cross talk" between electrodes, impeding long-term stability of LIBs.[3,4] Additionally, dendrite formation and resulting consumption of LE prevent the implementation of lithium metal as the anode. These drawbacks drive the development of rechargeable all-solid-state batteries (ASSBs),[5,6] where battery safety is enhanced by using a thermally stable solid electrolyte (SE). Moreover, ASSBs are promising systems for achieving both high energy, if lithium metal can be employed as anode material, and high power density, if interface impedances can be kept low.[7,8] However, as in the case of LIB a multitude of factors also impact the performance of SSBs. For instance, volume changes of active electrode materials can result in severe morphological and microstructural changes at the interfaces with the SE, leading to battery failure.[9–14] Engineering the microstructure, such as tuning ionic / electronic percolation paths in a composite cathode, can also affect the power and energy density of SSBs.[15–18]

Accordingly, the rate capability and cell lifetime of SSBs are closely linked to the stability and functioning of the electrode / SE interface. For the Li metal / SE interface, a mixed (electronic / ionic) conducting interphase (MCI) was proposed to describe the reaction between Li metal and LATP or LAGP as the SE,[19] which leads to a propagation of the interface and ultimately causes battery failure. Highly conductive SE, such as $Li_7P_3S_{11}$ and $Li_{10}GeP_2S_{12}$, are also unstable in contact with Li metal but appear to form favorable SEI in some cases.[20–24] Therefore, anodes with higher potential than Li metal have been used so far for the construction of ASSBs (e.g. indium metal,[15,25] $Li_4Ti_5O_{12}$[26,27] and graphite[28,29]) but with the corresponding disadvantage of lower specific energy and energy density than is potentially obtained with lithium metal.

The critical role of the cathode / SE interface has also been demonstrated, and the rate capability of ASSBs can be enhanced by modifying the interface between CAM and thiophosphate SEs by using a thin oxide layer, like $LiNbO_3$,[27,30] $Li_4Ti_5O_{12}$[31] or $LiNb_{0.5}Ta_{0.5}O_3$.[15] This effectively avoids mutual reactions at the interface and the potential formation of interphases with charge transport properties detrimental to cell performance.

Tackling these interfacial issues is challenging, given the complex chemical environment at the nanometer scale and accepting that first principle calculations have predicted inherent stability limitations for all thiophosphate SEs.[21] By using LGPS / carbon as model-type working electrode, LGPS was shown to be unstable at both high (> 2.1 V vs. Li^+ / Li) and low (< 1.7 V vs. Li^+ / Li) potentials.[32] It has also been shown that carbon additives facilitate SE decomposition at high voltages, resulting in highly oxidized sulfur species forming at the interface.[33]

In this work, we elucidate the factors limiting performance at the cathode / solid electrolyte interface within the composite cathode. A model ASSB was prepared using coated $LiCoO_2$ (denoted as c-$LiCoO_2$) as CAM, LGPS as SE, and indium as well as $Li_4Ti_5O_{12}$ as the anode active material. The results reveal: (i) c-$LiCoO_2$ particles exhibit mechanical failure after long-term electrochemical cycling in the SSB. (ii) Co diffusion is not fully suppressed by the coating layer. (iii) The SE and $LiCoO_2$ decompose within the operating potential range of $LiCoO_2$ during cycling, forming a lithium depletion layer at the interface that also contains Co, and acting as an effective barrier for charge transfer.

Our results reveal that mechanical failure and electrochemical instability of both active cathode material and solid electrolyte are highly relevant to the gradual capacity fading of solid-state batteries. The insight obtained serves as a guide for more critical evaluation of solid-state battery stability.

Experimental

Solid electrolyte. The solid electrolyte, $Li_{10}GeP_2S_{12}$ (LGPS), used in this work was synthesized as previously described.[15,24]

Cell Assembly. In this work, SSBs were assembled in a homemade cell casing, which has been shown in our previous work.[15] The SEM, ADF-STEM images and the XPS characterization results of the coating layer could be found in Supporting Information, Figure S1 and S2. First, 80 mg of the LGPS powder were filled into the PEEK (polyether ether ketone) cylinder and cold pressed with 1 t for 1 min (10 mm diameter). The composite cathode was prepared by mixing c-$LiCoO_2$ and SE in a weight ratio of 70 : 30 (corresponding to a volume ratio of 49 : 51) by hand. On one side of the pre-formed LGPS pellet, 10 mg of the composite cathode (corresponding to a loading of 1.1 mAh / cm^2) was spread, followed by uniaxial pressing with 3.5 t for 2 min. On the other side of the SE pellet, either a thin indium foil with a diameter of 8 mm (Alfa Aesar, 99.99 %, 0.125 mm in thickness), or 20 mg of composite anode with $Li_4Ti_5O_{12}$: SE : C65 = 30 : 60 : 10 wt%, was attached, and then pressed with 1.5 t for 2 min, serving as anode of the SSB. Two stainless steel rods were fixed by

screws to serve as current collectors. The total cell casing was subject to constant uniaxial pressure using the screw of an aluminum framework with 10 Nm torque (~ 70 MPa).

Electrochemical tests. Galvanostatic cycling of the cells was carried out in the voltage range of 2.0 – 3.6 V vs. In / InLi,[25] or 1.1 – 2.7 V vs. $Li_4Ti_5O_{12}$ / $Li_7Ti_5O_{12}$, which corresponds to about 2.6 – 4.2 V against Li^+ / Li. The theoretical capacity of $LiCoO_2$ was taken as 137 mAh / g, calculated based on $Li_{0.5}CoO_2$ in the fully charged state.[34,35] For all tests we used the VMP3 electrochemical workstation by Bio-Logic Science Instruments SAS. Electrochemical impedance spectroscopy (EIS) was carried out using the SP300 electrochemical workstation by Bio-Logic Science Instruments SAS. EIS spectra were always taken in the charged state (3.6 V vs. In / InLi) after selected cycles at 0.1 C. A rest period of 30 min was added before the EIS tests. An excitation voltage of 10 mV was chosen for measurements in the frequency range of 7 MHz – 10 mHz with 10 points per decade.

X-ray diffraction (XRD). X-ray diffraction was carried out with an Empyrean powder diffractometer (PANalytical, Netherlands) with Cu Kα radiation (λ_1 = 154.056 pm, λ_2 = 154.539 pm, I (λ_1 / λ_2 = 0.5). The cycled ASSB was disassembled inside the glovebox and the obtained pellet was sealed inside a silicon zero background sample holder covered with Kapton foil. All diffraction patterns were recorded in the 2θ range from 10 – 80 °, with a step size of 0.026 º and 300 s / step.

X-ray photoelectron spectroscopy (XPS). XPS measurements were carried out with a PHI Versaprobe II Scanning ESCA Microprobe (Physical Electronics PHI / ULVAC-PHI, USA) with a monochromatized Al K_α X-ray source (Beam area 200 µm × 1400 µm, X-ray power of 100 W). The pass energy of the analyzer was set to 23.5 eV for high-resolution spectra and to 187.6 eV for survey scans. For the pristine LGPS / LCO composite (without additional carbon) the C 1s signal from adventitious hydrocarbons was set to 284.8 eV to correct for charging effects. This resulted in a binding energy of 26.2 eV for the Ta $4f_{7/2}$ signal from the cathode coating layer (Ta^{5+}), which then was used as reference for all samples. All thiophosphate-containing samples were transferred under an argon atmosphere to the vacuum chamber with an air-tight sample transfer vessel. The sample holder was cooled with liquid nitrogen to low temperature ranges (−60 to −80 ºC) throughout the whole measurement process, in order to avoid possible sulfur evaporation from the SE. The CasaXPS software package (Version 2.3.17) was used for data analysis.

Scanning Transmission Electron Microscope (STEM). A small piece of composite cathode was removed from the solid-state cell in an argon filled glovebox, placed in a sample vial and crushed. Dry acetonitrile was added and the suspension was sonicated for 20 minutes to

disperse the powder. The sample was transferred to TEM copper grids by dropping the suspension onto the grid and evaporating the solvent. The copper grid was transferred to the TEM holder using a nitrogen filled glove bag and the TEM holder was inserted rapidly into the microscope, minimizing air exposure. Annular dark field images and electron energy loss spectra were recorded using an aberration-corrected ARM200F STEM/TEM operating at 200 kV. The ADF micrographs were taken using a converge semi-angle of 22 mrad and collection angles of 54 - 276 mrad.

Scanning Electron Microscope (SEM) Secondary electron images were recorded on a Zeiss Merlin microscope at 3 kV acceleration voltage. Samples were fixed on conducting adhesive tape in an argon filled glovebox and moved to the microscope using a transfer chamber to avoid exposure to air.

Results and discussions

I. Observing degradation of the model ASSB cell In / LGPS / c-$LiCoO_2$.

Cycling and CV: After 300 continuous cycles of the ASSB at 0.1 C, slow capacity fading down to 75 mAh / g is observed, which is 55% of its original capacity (Figure 1a). The overpotential (cell voltage at half SOC; state of charge) increased with cycle number, as is shown in the Supporting Information, Figure S3.

The degradation of the model ASSB is also demonstrated by the gradual peak broadening in the continuous cyclic voltammetry data (Figure 1c). Here, the 1-1' redox peaks correspond to the coexistence of two distinct hexagonal phases (I + II). The 2-2' and 3-3' redox peaks correspond to order-disorder processes and the phase transition between the hexagonal and monoclinic phases.[34,36] With increasing cycle number, the peak current of the first redox pair decreases, while the peak width increases. The other two redox pairs gradually become less pronounced and indistinguishable. It was reported from liquid electrolyte-LIBs (LE-LIBs)[37] that these phenomena may be associated with crystallite degradation and a change in the surface properties of the $LiCoO_2$ particles. Thus, the cycled c-$LiCoO_2$ particles were characterized in more detail by ADF-STEM and EELS (*vide infra*).

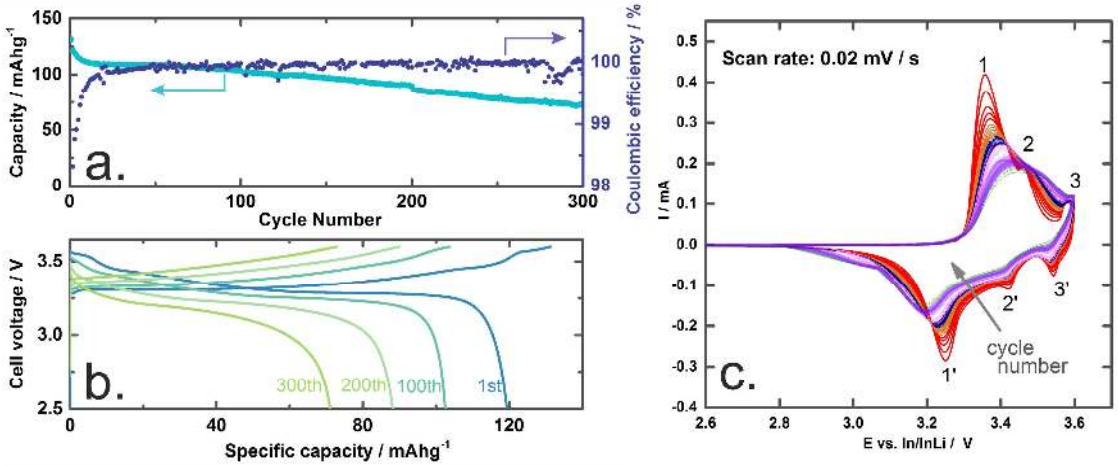

Figure 1: Degradation of the model ASSB cell upon galvanostatic cycling is observed by (a) capacity fading, (b) the increase in overpotential, and (c) the change in the cyclic voltammogram. In the CV results, with increasing cycle number, the peak current at 3.35 V decreases, accompanied by peak broadening. A gradual capacity fading is observed within 300 cycles at 0.1C.

Impedance spectroscopy: EIS results after 1 and 100 continuous galvanostatic cycles are compared in Figure 2. The total impedance increases by a factor of 5 after 100 cycles, reaching nearly 393 $\Omega \cdot cm^2$. All spectra were fitted with an equivalent circuit of the type

R(RQ)(RQ)(RQ)Q. HF, MF and LF were used to denote the semicircles in the high-frequency (~ MHz), mid-frequency (~ kHz) and low-frequency (~ 1 Hz) regions, respectively. In order to obtain data that can be compared with literature data, we converted resistances to area and polarization resistances in $\Omega \cdot cm^2$.

In the HF region, the semicircle diameter expands from 2 $\Omega \cdot cm^2$ to 157 $\Omega \cdot cm^2$. This change in the HF region is also clearly visible in the Bode plot (Supporting Information, Figure S4). Notably, the capacitance of the corresponding process decreases by three orders of magnitude from about 1.2 µF / cm^2 to about 0.001 µF / cm^2. The fitting parameters are shown in the Supporting Information, Table S1. Thus, the increased size of the HF semicircle suggests the growth of an interface resistance. As discussed below, the growth of a LGPS surface layer in the composite during cycling (i.e. the electrochemical decomposition of LGPS during cycling), may explain the HF impedance and the decreasing capacitance. If we assume that the capacitance depends reciprocally on the thickness of an interphase, this would point to a thickness increase by three orders of magnitude, e.g. from 1 nm to 1 µm. The XPS spectra further corroborate this result (*vide infra*). However, depending on the electronically conducting nature of the growing interphases the resulting thickness will vary.

Additionally, the MF semicircle also increases in size and reaches 118 $\Omega \cdot cm^2$ after 100 cycles (starting from 19 $\Omega \cdot cm^2$, with a gradually decreasing characteristic frequency from about 5 kHz to about 4 kHz), leading to the capacitance decreasing from 9.3 µF / cm^2 to 1.8 µF / cm^2. In our previous study,[15] we interpreted this semicircle as response of the cathode / SE interface, and we will discuss this below in more detail. The response in the LF region increases from 11 $\Omega \cdot cm^2$ to 93 $\Omega \cdot cm^2$ after 100 cycles, which is ~ 5 times higher than after the 1st charge, and again, the characteristic frequency changes slightly from about 9.5 Hz to 6.5 Hz (capacitance from about 9.6 mF / cm^2 to 1.7 mF / cm^2). In our previous work,[9] we interpreted the LF response as the interfacial resistance between indium and the SE. It is related to the limited reversibility of the $InLi_{1-x}$ intermetallic phase which is deleterious to the cycle stability of the SSB.

Summarizing the impedance results, we find that the spectra change quantitatively with time, but can be well described by the same equivalent circuit. The characteristic frequencies decrease with time and all area-specific capacitances decrease with time, too. By and large, this gives evidence that all three processes are related to the kinetics of interfaces. The decreasing capacitances indicate the growth or widening of the corresponding interfaces, which we will further substantiate below.

Summary of electrical characterization: In short, we observed in the electrochemical measurements, i) characteristic peak evolutions in the CV; ii) an increase in overpotential and decrease of capacity in the charge-discharge curves; iii) increase of impedance in both high and middle frequency range in the EIS, and a decrease of all capacitance contributions. Together, these data indicate that the ASSB has gradually degraded with continuous cycling, forming wider and more resistive interfaces / interphases. In the following sections, we will demonstrate post-mortem analytical results from various characterizations, in order to provide insight into the underlying degradation mechanisms.

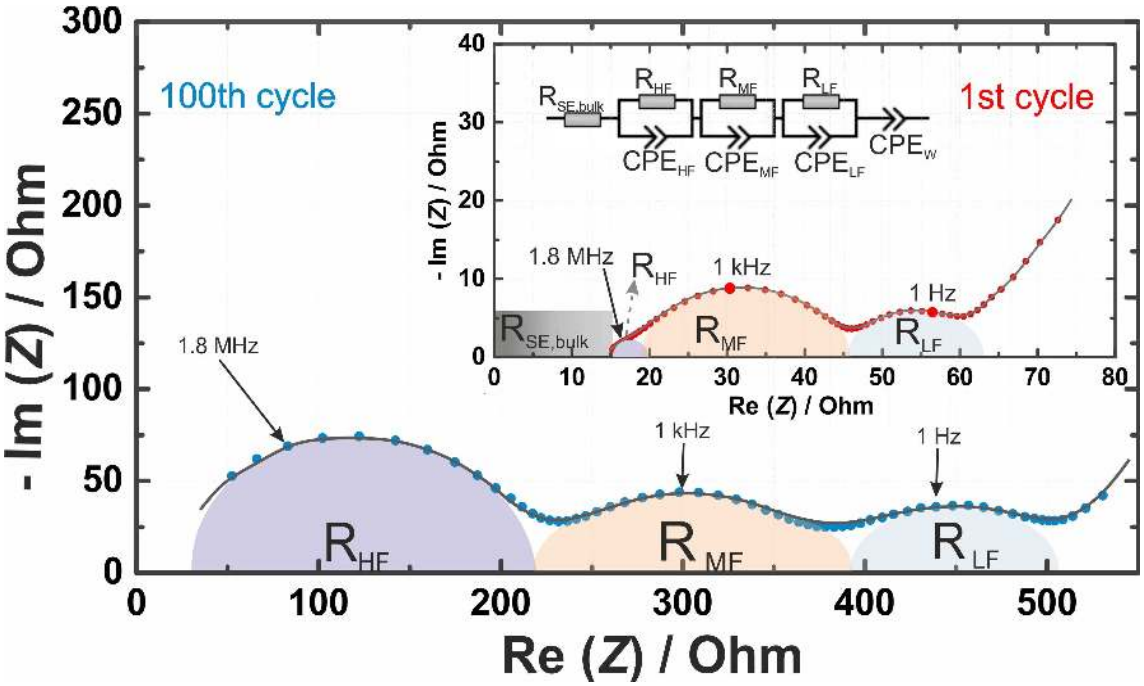

Figure 2: Impedance (Nyquist plots) of the model ASSB after the 1st (small insert) and 100th charge. The increase of the semicircle in the HF region indicates solid electrolyte decomposition (such as grain-boundary deterioration) during cycling. Meanwhile, the semicircles in the MF and LF regions increase after 100 cycles, indicating the instability of the cathode / SE interface.

II. Macroscopic change and chemical instability of active material particles.

Electron microscopy: In order to better understand the degradation of crystalline c-$LiCoO_2$ in the SSB, macroscopic changes of the cycled c-$LiCoO_2$ particles were first monitored by means of SEM and ADF-STEM, and compared with uncycled c-$LiCoO_2$ particles (Figure 3). Before cycling, c-$LiCoO_2$ exists as mostly uniform single particles and particle aggregates. The particle surface appears coarse due to the coating layer. However, after 300 cycles at 0.1 C, local mechanical failures induced by electrochemical cycling are directly evidenced by the fracture and shear of c-$LiCoO_2$ particles, shown in Figure 3b, 3d and 3e, as well as in the Supporting Information Figure S5.

In the SEM images, some cycled particles show an abrupt change in the surface morphology toward their edges. Additionally, some of the edges appear to separate the adjacent coated and uncoated surfaces. This likely indicates that the particle fracturing occurs during cycling, thereby exposing pristine c-$LiCoO_2$ surfaces from previously coated surfaces (after disassembly). Moreover, some cycled particles exhibit a staircase-like morphology, probably resulting from a gliding shift of crystalline layers (shear) along the basal plane during cycling, as shown in Figure 3e. We observed this structural feature far less in pristine particles. The shear bands at the surfaces suggests that some c-$LiCoO_2$ particles have experienced severe mechanical deformation, resulting in shear of particle segments. The shear of c-$LiCoO_2$ is further supported by the ADF-STEM images of c-$LiCoO_2$ particles after electrochemical cycling (Figure 3d). In contrast to the bulk particles, the cycled materials contained significant fractions of smaller, thinner platelet-like crystallites. This shows that two identically shaped segments are shifted with respect to each other along the basal plane, indicating that both segments originate from the same particle.

In LE-LIBs, structural failure has also been observed, but this did not necessarily lead to rapid capacity fading.[38] In LE-LIBs, the liquid electrolyte around the $LiCoO_2$ provides enough ionic transport to the active particles by simply penetrating into the generated microcracks, ensuring continuous Li^+ percolation paths. However, in SSBs, the rigid SE cannot flow plastically into formed microcracks. The loss of capacity from the cracked $LiCoO_2$ particles accelerates capacity fading. Additionally, accompanied by the lattice strain in the active materials, brittle fracture of the SE can occur under low stresses, due to the low fracture toughness (0.23 ± 0.04MPa $m^{1/2}$) of the xLi_2S-yP_2S_5 family.[39]

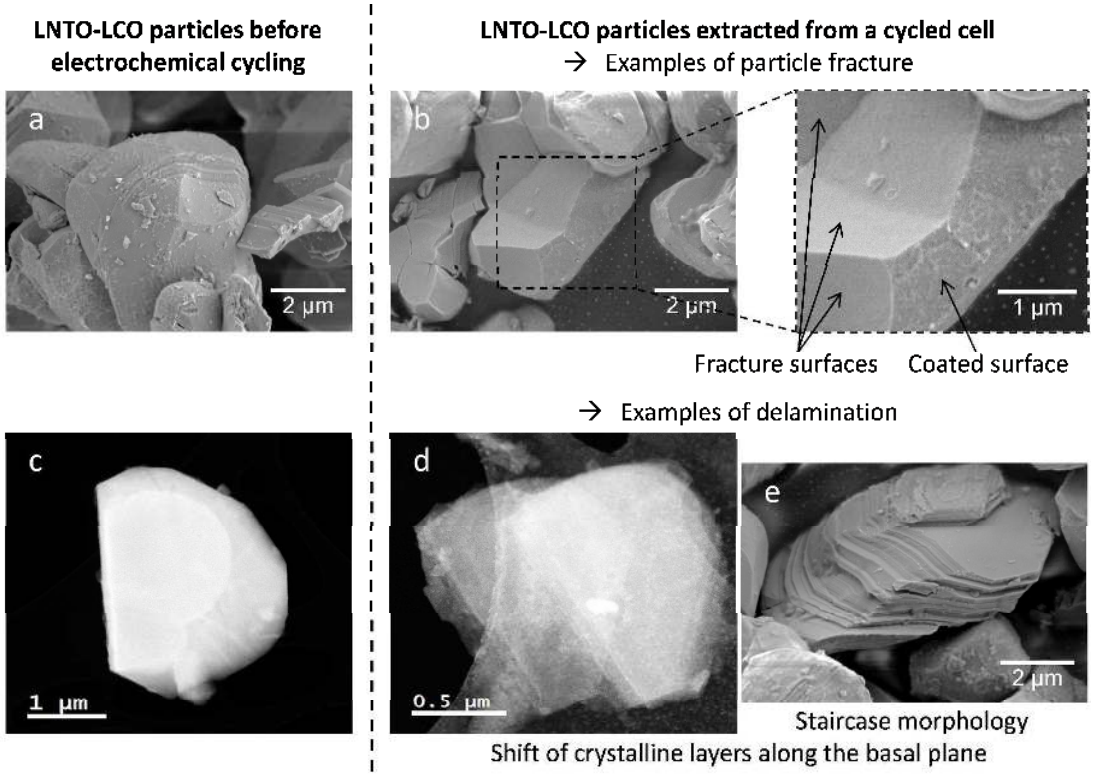

Figure 3: (a, b, e) SEM and (c, d) low magnifications ADF-STEM images of pristine c-$LiCoO_2$ particles (a, c) before cycling, (b, e) c-$LiCoO_2$ particles extracted from cells after 300 cycles and (d) after 110 cycles.

Electron energy loss spectroscopy (EELS): The inherent instability of the interface between $LiCoO_2$ and the thiophosphate SE was predicted by computational studies and mutual elemental diffusion is one of the consequences (e.g. the energetically preferable Co ↔ P exchange).[40] Here, even though coating helped to maintain the integrity of $LiCoO_2$ crystals during cycling, Co diffusion to the surface of $LiCoO_2$ is detected by means of EELS. As shown in Figure 4a, the coating layer could be well observed in both cases using HR-STEM. An EELS line scan of both Co $L_{2,3}$ and O *K*-edges was carried out and the elemental profiles are shown below the high-resolution ADF-STEM images. In the pristine c-$LiCoO_2$ particle, Co was only detected in the $LiCoO_2$ bulk and no significant signal could be detected in the coating layer, which implies that the coating and the subsequent cold pressing process did not cause Co diffusion into the coating layer. However, in the case of the c-$LiCoO_2$ particles after 100 cycles, Co enrichment was found in the surface layer of $LiCoO_2$. Such interdiffusion of Co hence occurs even at room temperature. This result clearly demonstrates that the coating layer could not completely suppress Co diffusion during long galvanostatic cycling. The Co diffusion, on the one hand, directly leads to a small mass decrease in the active material. On the other hand, it may form electronically conductive compounds with LGPS, such as CoS,

providing extra electronic conduction paths and possibly favoring further SE decomposition, similar to carbons.[33] More information of the ADF-STEM and the EELS spectra of $LiCoO_2$ can be found in Supporting Information, Figure S6 and S7.

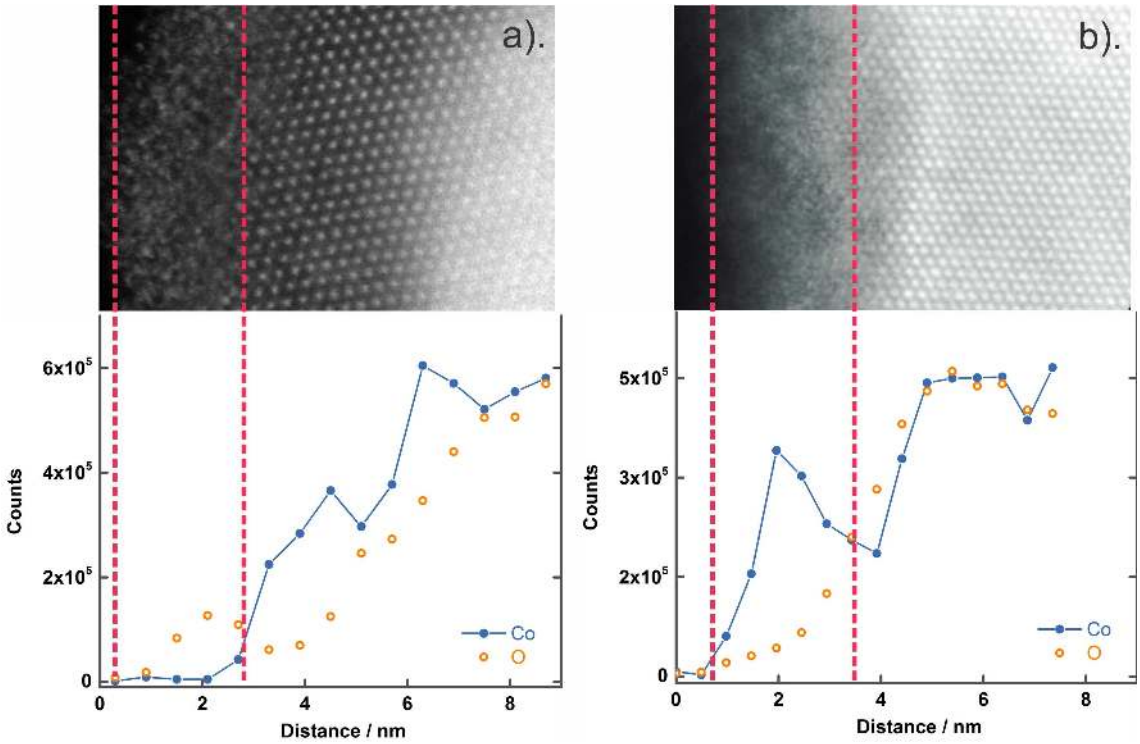

Figure 4: (a) High-resolution ADF-STEM image of a pristine c-$LiCoO_2$ particle taken along the [211] zone axis and corresponding EELS line-scan shown below. The Co signal is very low in the coating layer, indicating that the coating process does not lead to significant Co diffusion from the bulk $LiCoO_2$ into the coating layer. (b) High resolution ADF-STEM image of the c-$LiCoO_2$ particle cycled 300 times, taken along the [211] direction and the corresponding EELS line scan shown below. Even though the coating layer could still be seen, the Co signal detected in the layer is now significant, which indicates Co diffusion into the coating layer after galvanostatic cycling.

X-ray diffraction: Figure 5a shows the X-ray diffractogram of the c-$LiCoO_2$ / LGPS (70:30 wt%) composite in a pristine SSB and in a SSB after 100 cycles. All of the reflections can be assigned to c-$LiCoO_2$ and LGPS. For both c-$LiCoO_2$ and LGPS, reflection-broadening is observed after cycling, as shown in the inserts. A minor shift of the reflections can be found due to small variations in the cell thickness, leading to an additional sample displacement in the Bragg-Brentano geometry. A Pawley refinement indicates no change in the lattice parameters of both LGPS and LCO.

In order to gain more information about the crystallite size and microstrain, a Williamson-Hall plot was evaluated for c-$LiCoO_2$ and shown in Figure 5b. The selected reflections in different orientations were fitted with a pseudo-Voigt function and the corresponding FWHM was determined based on the fittings. An increase in the intercept is

shown for cycled c-$LiCoO_2$. Given that higher intercept values refer to smaller grain size, the cycled c-$LiCoO_2$ exhibits a smaller grain size. In fact, microstructural changes in single crystalline $LiCoO_2$ in a SSB was revealed by Gong et al. using *in situ* STEM.[41].

It should be noted that even though reflection-broadening was also observed for LGPS, the Williamson-Hall plot cannot be constructed, as a severe scattering of data points is found. In fact, the asymmetric reflection-broadening of LGPS indicates the formation of a second phase as an interface layer after cycling. For gathering more information about the decomposition reaction of LGPS, XPS was carried out for cells disassembled with an increasing number of cycles.

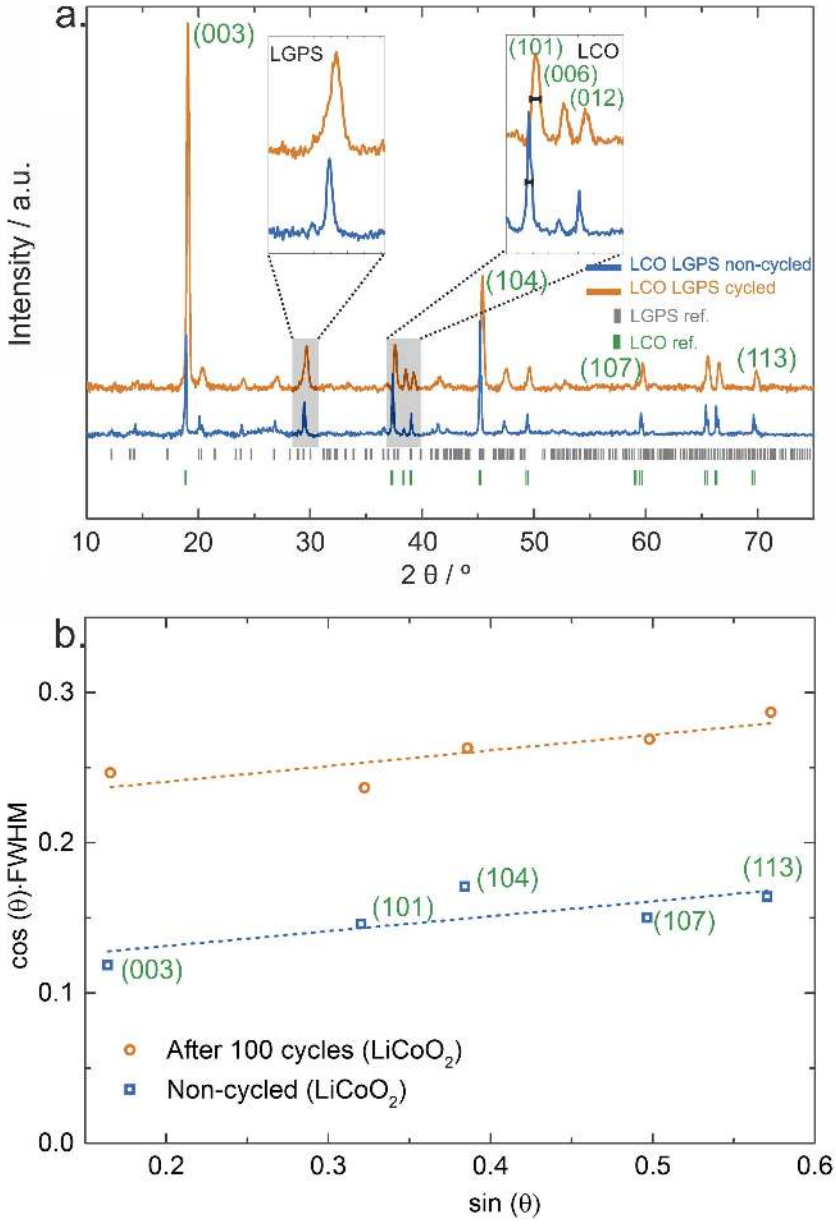

Figure 5: (a) The comparison of X-ray diffractograms of $LiCoO_2$ / LGPS composites (70:30 wt%), before (blue) and after 100 cycles (orange). The cycled SSB were disassembled in the

charged state (i.e. delithiated $LiCoO_2$). Reflection-broadening is observed for both $LiCoO_2$ and LGPS after cycling (as shown in the inserts). (b) Williamson-Hall plot for $LiCoO_2$ pristine (blue) and after 100 cycles (orange). An increase in the intercept was observed after cycling, indicating the decrease in grain size of $LiCoO_2$. The similar slope in both cases indicates that the crystalline strain remains intact after cycling. No linear relation was found for LGPS. Thus, the asymmetric reflection-broadening of LGPS might be due to additional phases induced by decomposition during cycling.

III. Interfacial reactions of composite electrodes

X-ray photoelectron spectroscopy: In order to get more chemical information on the decomposition reactions at the LGPS / c-$LiCoO_2$ interface, XPS was used for post-mortem analysis of the pellets' surface of both the pristine and cycled composite cathode. As shown in Figure 6, the photoemission lines of S 2p, P 2p and Ge 3d were recorded for pristine LGPS (c-$LiCoO_2$ / LGPS) and for the composite cathode which was extracted from the SSB after various cycles. The fit parameters are summarized in the Supporting Information, Table S3. In the pristine, mechanically mixed c-$LiCoO_2$ / LGPS composite, one peak doublet at 161.3 eV (S $2p_{3/2}$), representing the (P/Ge)-S-Li bond of LGPS, can be fit to the main part of the S 2p signal, which is in agreement with previous results from our group.[42] The S 2p spectrum of a pure LGPS sample is also provided as reference. Even though a weak additional signal on the high binding energy side is also present in the mixture, no evidence of chemical reactions after direct mixing between coated $LiCoO_2$ and LGPS was found. As expected from the crystal structure of LGPS, deconvolution of the P 2p and Ge 3d signals of the uncycled cathode composite is straightforward by assuming a single chemical state (i.e. PS_4^{3-} at 131.8 eV and GeS_4^{4-} at 30.8 eV).

Significant signal broadening toward higher binding energies in the high-resolution XPS spectra of all elements contained in the SE reveals degradation. Generally, peak broadening towards higher binding energies can be attributed to a decrease in the local charge density, i.e. oxidation, and such oxidation is to be expended in contact with the high voltage $LiCoO_2$ cathode.[43] These changes are most evident in the high-resolution S 2p spectra and a satisfying fit result was obtained by modelling the main signal with four peak doublets, denoted as: (P/Ge)–S (161.3 eV, blue), A (162.3 eV, brown), B (163.3 eV, pale red), and –S–S– (163.9 eV/ 164.6 eV, orange).

After the 1st cycle, signal broadening has occurred due to the formation of A and B. One should note that there is a wide variety of possible decomposition products at the c-$LiCoO_2$ / LGPS interface, many of them with binding energies quite close to each other. We

expect the underlying sulfur chemistry to be rich, due to the tendency of sulfur to form polysulfides. This, however, cannot be resolved by XPS and we can only speculate on the origin of the new sulfur signals of oxidized species (i.e. A and B). These lines may be attributed to LGPS decomposition products such as germanium sulfide (GeS_2),[44–46] or to terminal sulfur groups of Li_2S_n,[48] P–S–$(S–)_n$ [47,49,50] like polysulfide species with different chain lengths, disordered species containing –P–S–P– (–Ge–S–P– or–Ge–S–Ge–) or to P/Ge=S bonds.[51] Among them, the –S–S– bond formed between the PS_4 units by oxidation is quite likely, as the binding energy matches well with the reported value of 162.7 eV.[49] The polymerization of PS_4 is indeed energetically favorable, as recently predicted by computational results and also experimentally demonstrated.[50,52]

In addition, it seems likely that cobalt sulfides and/or thiosulfates have also formed at the c-$LiCoO_2$ / LPGS interface, as cobalt diffuses from bulk c-$LiCoO_2$ into the coating layer. However, due to the strong overlap of signals, we cannot unambiguously identify this compound solely with XPS. Nevertheless, the interface (or interphase) formed by these compounds is likely to be responsible for the observed impedance in the MF region after the 1st and last cycle (Figure 2).

With increasing cycle numbers, the S 2p peaks become broader. For longer polysulfide chain lengths, the influence of the terminal lithium (or phosphorus) atom is reduced (i.e. the charge density decreases) resulting in a higher binding energy for the bridging sulfur atoms. Furthermore, a S $2p_{3/2}$ binding energy of 164 eV – 164.5 eV is frequently reported for elemental sulfur.

On the other hand, the accumulation of oxidative changes is also apparent in both the P 2p and Ge 3d high-resolution spectra. In these regions, the signal intensities are much smaller, leading to larger uncertainties in the peak modelling. A second component at higher binding energies, denoted as C at 133.3 eV, is present in the P 2p spectra, which may be attributed to –P–S–P– or –Ge–S–P– bonds. Similar results are found in the Ge 3d spectra: Two new components at 31.5 eV (E) and 32.4 eV (F) are required for fitting the spectra of cycled samples. While the signal could be attributed to germanium sulfide,[44] it is more likely related to oxide species (GeO_2).[45]

In all of the samples studied herein, the reduction of P or Ge is not detected, as one would expect. Thus, the degradation of LGPS only involves oxidation reactions, which is not surprising in view of the oxidizing conditions in general in the cathode. In reviewing the framework structure of LGPS and the various thiophosphates in the Li–P–S ternary system, we find that two PS_4^{3-} units (which are the main building units that form the LGPS

framework) can form elemental sulfur accompanied by the formation of $P_2S_6^{2-}$ anions (which contain –P–S–P– bonds) in which the oxidation state of P^{5+} is maintained. This reaction is supported by the XPS results of pure $Li_2P_2S_6$ (see Supporting Information, Figure S9).

In the spectrum, the main component of sulfur in the –P–S–P– bond lies in regions A and B. The phosphorous spectrum of $Li_2P_2S_6$ also covers the area of C, namely at higher binding energies than $Li_{10}GeP_2S_{12}$. The structure of $Li_2P_2S_6$ has been recently analyzed and published in another paper from our group.[53] In accordance with the electronegativity difference, a general trend of the binding energy sequence is as follows: $E_B(S_0) > E_B(–S–S–) > E_B(–P–S–P–) > E_B(–S–P / Ge)$.

It was reported in literature, that Li can be electrochemically extracted from LGPS above the potential of 1.8 V vs. In / InLi,.[21,32] The voltage for inserting Li into the bulk SE is lower than 1.6 V vs. In / InLi.[21,32] Thus, in SSBs with $LiCoO_2$ as CAM, the operation potential range (2.0 – 3.6 V vs. In / InLi) allows for the extraction of Li from LGPS, but is not sufficient for the insertion of Li into LGPS at low potentials. In other words, a Li depleted layer forms during charging, representing oxidation of LGPS. This is suggested by the low first cycle efficiency of all of the assembled SSBs and the low coulombic efficiency in the first 10 cycles (Figure 1). Since the Li-depleted layer deviates from the ideal structure of LGPS, and $Li_2P_2S_6$ shows a very low ionic conductivity in the range of 10^{-8} S/cm, the formation and growth of this layer generates a barrier to the Li-ion mobility, resulting in the increase in internal resistance and cell overvoltage (Figure 2). Also, due to the limited ionic (and electronic) conductivity of the decomposition products, the decomposition reaction is kinetically limited once the layer is formed. Thus, the major part of the Li depletion layer probably forms within the first 10 cycles. In the following cycles, accumulative decomposition of LGPS is observed. This indicates the electronically conductive character of the components at the interface, which provide electronic paths through the interface to the active material. Given that Co is detected in the coating layer after cycling (Figure 4b), one may speculate that the electronic paths could be formed by compounds such as CoS at the interface. On the other hand, GeS_2 formed at the interface may also provide electronic conductivity.

From the 10^{th} cycle on, signals above 165 eV were detected, which can be clearly attributed to an oxide environment and indicate the participation of oxygen in the decomposition reactions. Possible oxygen sources are the oxide coating and $LiCoO_2$. The participation of oxygen in the degradation reactions correlates well with the structural

degradation of $LiCoO_2$, as observed by STEM. Clearly, a detailed decomposition scenario is speculative at this point, but the formation of resistive interphases is evident.

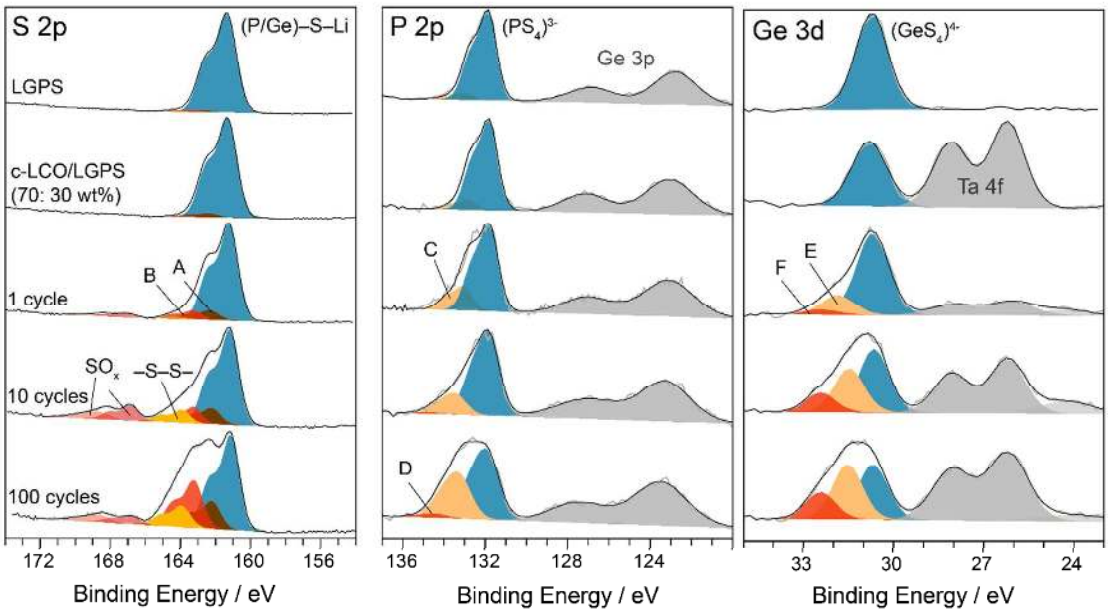

Figure 6: XPS characterization of the model SSB cathode recorded after different cycle numbers. From top to bottom, the photoemission lines of S 2p, P 2p and Ge 3d were collected for pristine LGPS, pristine c-$LiCoO_2$ / LGPS mixtures (which have been stored for 3 months before measurement), and the cathode material after the 1st charge, 10th charge and 100th charge. The S 2p peak of the cycled LGPS in the composite cathode becomes broader and shifts toward higher binding energy, indicating that sulfur in the LGPS is oxidized after electrochemical cycling. With increasing cycle numbers, oxidized sulfur components accumulate, indicating the unstable nature of the interface. Moreover, the fractions of highly oxidized components -S-S- and B become more pronounced. At the same time, line broadening of P 2p and Ge 3d towards higher binding energy is also observed.

SE decomposition controlled by cell voltage: A full cell test. In order to further investigate the influence of the cell voltage on the stability of the SE (i.e. to directly compare the decomposition products at both the cathode and anode sides), a LTO / LGPS / c-$LiCoO_2$ full cell was assembled and cycled galvanostatically. A post-mortem XPS analysis was carried out after the 15th charge (Figure 7). The cycling performance as well as the EIS results can be found in Supporting Information Figure S10.

A post-mortem XPS analysis of the cathode, SE and anode allows direct comparison of the degradation of LGPS on both sides of the cell. As expected, the spectrum of LGPS used as the separator is identical to pristine LGPS (Figure 7). Notable peak broadening is observed on the cathode side, which corresponds well with the spectrum detected in the half cell with In as anode (Figure 6). Highly oxidized species such as S^0 are detected.

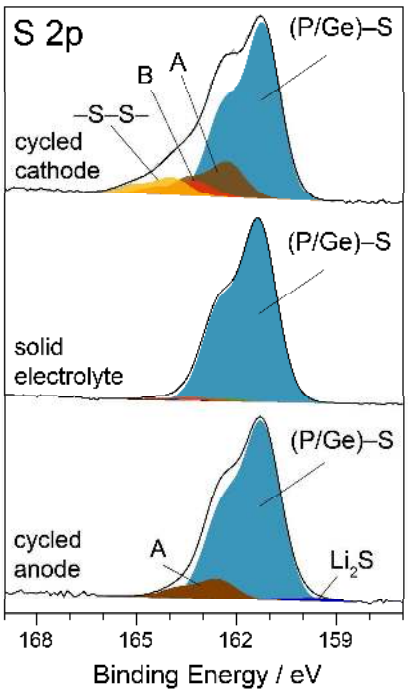

Figure 7: XPS results for LGPS in different parts of the SSB full cell: LTO / LGPS / c-$LiCoO_2$, measured after 15th cycles. On the cathode side, severely oxidized S is observed, reflected by line broadening and shift toward higher binding energies. Less line changes were observed at the anode side with LTO as active material, as compared to the S2p signal of pristine LGPS. Clearly high potentials favor the decomposition of LGPS.

Compared to the cathode, the anode side shows only minor degradation effects. Only a small fraction of component A is detected, even though 10 wt% carbon is used as an additive in the anode (carbon has been proven to cause severe decomposition of LGPS at the cathode side).[33] In addition, Li_2S was detected at 160 eV on the anode side. This result agrees well with previous computational results.[22,32] We can conclude that at the anode side, LGPS also experiences decomposition, forming products similar to polymerized PS_4 ions (i.e. the –S–S– bonds formed between the PS_4 unit). Furthermore, under reducing conditions, the formation of Li_2S is favored. Since Li_2S is (weakly) ion-conducting but electronically insulating, further decomposition of LGPS at the anode side is kinetically limited. Thus, the LGPS decomposition is potential driven, which is more severe at the cathode side (at higher potential) than at the anode side (at lower potential), which corresponds well with that reported in literature.[52,54]

IV Discussion.

Figure 8 schematically describes the three relevant situations that may occur in the cathode composed of c-$LiCoO_2$ and SE during long term cycling. In situation I, an ideal and well covering coating layer (with sufficient ionic conductivity) is maintained during cycling. The

c-$LiCoO_2$ has intimate contact with the SE and Li ions can be transferred reversibly between $LiCoO_2$ and the SE, while the electrons are transferred through the external circuit. This situation is beneficial for a practical SSB with long cycle stability. In situation II, c-$LiCoO_2$ is isolated from the SE due to inhomogeneous mixing of the composite cathode or due to contact loss after volume changes in c-$LiCoO_2$.[9] In these areas, both electrons and Li ions cannot be transferred due to the lack of percolation paths. The "dead" material leads not only to direct capacity fading, but to a locally strongly non-uniform current distribution and correspondingly non-uniform strain. In situation III, the SE decomposes at high voltages due to its limited electrochemical stability window. A Li depletion layer will then form at the interface, resulting in higher internal resistances from the formation of decomposition products. When electronically conductive components accumulate at the interface, the Li depletion layer can gradually grow, further reducing the Li ion mobility and leading to more severe capacity fading.

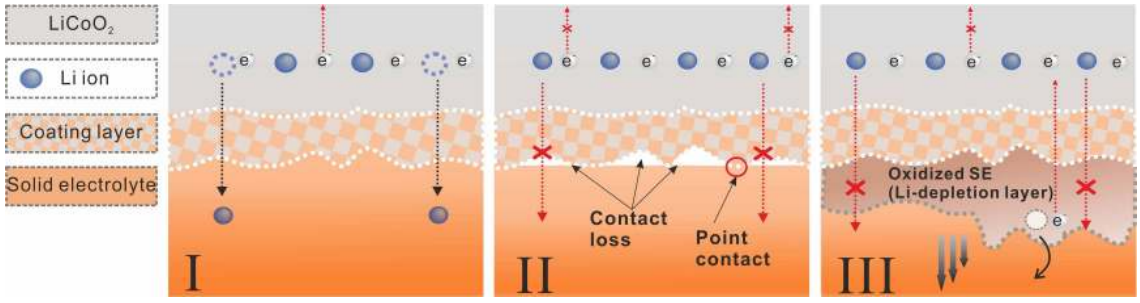

Figure 8: Schematic description of three possible situations occurring in a model SSB with $LiCoO_2$ as the active material and LGPS as the SE. I: The ideal case. Intimate contact between the SE and c-$LiCoO_2$, and no mutual reaction or decomposition of the SE. II: Contact loss due to volume changes or failures during preparation. III: Decomposition of the SE at high voltages, forming a Li^+-depletion layer, thereby inhibiting Li^+ mobility.

Going back to the initial discussion of the impedance results, our interpretation of the impedance growth in the three well separated frequency regions (HF, MF and LF) is supported by the microscopic and spectroscopic results. We assign the LF response to the indium electrode, and both MF and HF response are then caused by the cathode composite. Both MF and HF impedance grow and show increasing resistance and decreasing capacitance, which can be interpreted as growth of resistive interphases or widening of resistive interfaces. While the unequivocal assignment is not possible yet, the degradation of LGPS and the formation of a resistive decomposition layer will be responsible for one of the two responses – most probably the MF response. The high frequency response may then represent the

impedance of the LCO / coating interface / interphase and reactions therein. Further studies need to give more evidence for this interpretation.

Conclusion

In this paper, multiple degradation phenomena in a model SSB were observed after long-term cycling tests, despite the use of a thin oxide coating layer for LCO. Shear and particle fractures of $LiCoO_2$ were detected by STEM and illustrate the mechanical failure of $LiCoO_2$ after repeated volumetric changes. A decrease in the grain size of cycled $LiCoO_2$ was revealed by Williamson-Hall plots derived from the X-ray diffraction patterns. Although the latter monitors changes on a much smaller length scale than the former, both reflect mechanical failure of $LiCoO_2$. Electrochemically induced reaction between $LiCoO_2$ and LGPS, likely arising from only partial surface coating on $LiCoO_2$, results in degradation and formation of a surface layer containing Co revealing inherent structural instability of $LiCoO_2$, which cannot be completely suppressed with the coating layer.

With regard to the SE, electrochemical degradation of LGPS is observed upon charging. The formation of –S–S– bonds between PS_4 units, and the formation of $Li_2P_2S_6$ and S^0 are energetically favored. Meanwhile, Li is extracted from LGPS and participates in the electrochemical reaction during charging. The formed Li depletion layer at the interface largely hinders the Li ion mobility, leading to higher internal resistances. The evolution of EIS and XPS spectra with cycling indicates a mixed conducting (electronic/ionic) character for the decomposition products, which allows for further oxidization of LGPS with longer cycling time. In assessing the impedance data, one may speculate that components A and B (i.e. the –S–S– bond formed between PS_4) are responsible for the observed interfacial process in the MF range, while the accumulation of highly oxidized sulfur significantly contributes to the interfacial process in the HF range. On the anode side, the $Li_4Ti_5O_{12}$ / LGPS composites show minor degradation after cycling, revealing that the decomposition of LGPS is closely related to the electrochemical potential applied.

This work provides insight into the underlying degradation mechanisms of SSBs, which are rooted in the electrochemical decomposition of the cell components. The results also yield important implications for the design of zero-strain materials, in order to mitigate mechanical damages. Future studies need to focus to the development of SEs with larger electrochemical stability windows and on the engineering of stable interfaces within SSBs. Obviously, our understanding of the mechanistic details is still in an early state, and further studies are required to achieve a more complete picture.

ASSOCIATED CONTENT

Supporting Information

The supporting information includes: SEM and ADF-STEM images of bare and coated $LiCoO_2$ particles. XPS spectra of coated $LiCoO_2$. Overvoltage as a function of cycle numbers of a model SSB. Bode plot of a model SSB after 1st and 100th charge. SEM images of pristine c-$LiCoO_2$ particles. ADF-STEM images of the surface of bare $LiCoO_2$ and c-$LiCoO_2$. EELS spectra from the surface of bare $LiCoO_2$ and the surface of c-$LiCoO_2$. Raman spectroscopy of fresh and cycled composite cathode. XPS spectra of pure $Li_2P_2S_6$. Electrochemical characterization of LTO / LGPS / c-$LiCoO_2$ full cell. Parameters used for EIS fitting and XPS fitting.

AUTHOR INFORMATION

Corresponding Authors

*wolfgang.g.zeier@phys.chemie.uni-giessen.de; *juergen.janek@phys.chemie.uni-giessen.de

Notes

The authors declare no competing financial interests.

ACKNOWLEDGMENT

The authors acknowledge financial support within the BASF Scientific Network for Electrochemistry and Batteries. This project was further supported by the Laboratory of Materials Research (LaMa) of JLU and by the HGP-E. The authors thank Dr. Dominik. A. Weber and Raimund Koerver for helpful discussion. The authors thank, J. Kulisch and P. Hartmann for helpful discussions and scientific support. Fruitful discussion within the BASF Scientific Network for Electrochemistry and Batteries is highly appreciated.

REFERENCES

(1) Goodenough, J. B. Rechargeable Batteries: Challenges Old and New. *J. Solid State Electrochem.* **2012**, *16*, 2019–2029.

(2) Goodenough, J. B.; Kim, Y. Challenges for Rechargeable Li Batteries. *Chem. Mater.* **2010**, *22*, 587–603.

(3) Michalak, B.; Sommer, H.; Mannes, D.; Kaestner, A.; Brezesinski, T.; Janek, J. Gas Evolution in Operating Lithium-Ion Batteries Studied In Situ by Neutron Imaging. *Sci. Rep.* **2015**, *5*, 15627.

(4) Michalak, B.; Berkes, B. B.; Sommer, H.; Bergfeldt, T.; Brezesinski, T.; Janek, J. Gas Evolution in $LiNi_{0.5}Mn_{1.5}O_4$/Graphite Cells Studied In Operando by a Combination of Differential Electrochemical Mass Spectrometry, Neutron Imaging, and Pressure Measurements. *Anal. Chem.* **2016**, *88*, 2877–2883.

(5) Janek, J.; Zeier, W. G. A Solid Future for Battery Development. *Nat. Energy* **2016**, *1*, 16141.

(6) Hu, Y.-S. Batteries: Getting Solid. *Nat. Energy* **2016**, *1*, 16042.

(7) Zeng, X.-X.; Yin, Y.-X.; Shi, Y.; Zhang, X.-D.; Yao, H.-R.; Wen, R.; Wu, X.-W.; Guo, Y.-G. Lithiation-Derived Repellent toward Lithium Anode Safeguard in Quasi-Solid Batteries. *Chem* **2018**, *4*, 298–307.

(8) Duan, H.; Yin, Y. X.; Shi, Y.; Wang, P. F.; Zhang, X. D.; Yang, C. P.; Shi, J. L.; Wen, R.; Guo, Y. G.; Wan, L. J. Dendrite-Free Li-Metal Battery Enabled by a Thin Asymmetric Solid Electrolyte with Engineered Layers. *J. Am. Chem. Soc.* **2018**, *140*, 82–85.

(9) Zhang, W.; Schröder, D.; Arlt, T.; Manke, I.; Koerver, R.; Pinedo, R.; Weber, D. A.; Sann, J.; Zeier, W. G.; Janek, J. (Electro)chemical Expansion during Cycling: Monitoring the Pressure Changes in Operating Solid-State Lithium Batteries. *J. Mater. Chem. A* **2017**, *5*, 9929–9936.

(10) Piper, D. M.; Yersak, T. A.; Lee, S.-H. Performance of Silicon Anodes Effect of Compressive Stress on Electrochemical Service Email Alerting Effect of Compressive Stress on Electrochemical Performance of Silicon Anodes. *J. Electrochem. Soc. J. Electrochem. Soc.* **2013**, *160160*, 77–81.

(11) Koerver, R.; Aygün, I.; Leichtweiß, T.; Dietrich, C.; Zhang, W.; Binder, J. O.; Hartmann, P.; Zeier, W. G.; Janek, J. Capacity Fade in Solid-State Batteries: Interphase Formation and Chemomechanical Processes in Nickel-Rich Layered Oxide Cathodes and Lithium Thiophosphate Solid Electrolytes. *Chem. Mater.* **2017**, *29*, 5574–5582.

(12) Grenier, A.; Liu, H.; Wiaderek, K. M.; Lebens-Higgins, Z. W.; Borkiewicz, O. J.; Piper, L. F. J.; Chupas, P. J.; Chapman, K. W. Reaction Heterogeneity in $LiNi_{0.8}Co_{0.15}Al_{0.05}O_2$ Induced by Surface Layer. *Chem. Mater.* **2017**, *29*, 7345–7352.

(13) Liu, H.; Wolf, M.; Karki, K.; Yu, Y. S.; Stach, E. A.; Cabana, J.; Chapman, K. W.; Chupas, P. J. Intergranular Cracking as a Major Cause of Long-Term Capacity Fading of Layered Cathodes. *Nano Lett.* **2017**, *17*, 3452–3457.

(14) Radin, M. D.; Alvarado, J.; Meng, Y. S.; Van Der Ven, A. Role of Crystal Symmetry in the Reversibility of Stacking-Sequence Changes in Layered Intercalation Electrodes.

Nano Lett. **2017**, *17*, 7789–7795.

(15) Zhang, W.; Weber, D. A.; Weigand, H.; Arlt, T.; Manke, I.; Schröder, D.; Koerver, R.; Leichtweiss, T.; Hartmann, P.; Zeier, W. G.; Janek, J. Interfacial Processes and Influence of Composite Cathode Microstructure Controlling the Performance of All-Solid-State Lithium Batteries. *ACS Appl. Mater. Interfaces* **2017**, *9*, 17835–17845.

(16) Mizuno, F.; Hayashi, A.; Tadanaga, K.; Tatsumisago, M. Effects of Conductive Additives in Composite Positive Electrodes on Charge-Discharge Behaviors of All-Solid-State Lithium Secondary Batteries. *J. Electrochem. Soc.* **2005**, *152*, A1499.

(17) Nagao, M.; Hayashi, A.; Tatsumisago, M. Fabrication of Favorable Interface between Sulfide Solid Electrolyte and Li Metal Electrode for Bulk-Type Solid-State Li/S Battery (Li Thin Film as Anode). *Electrochem. Commun.* **2012**, *22*, 177–180.

(18) Strauss, F.; Bartsch, T.; De Biasi, L.; Kim, A. Y.; Janek, J.; Hartmann, P.; Brezesinski, T. Impact of Cathode Material Particle Size on the Capacity of Bulk-Type All-Solid-State Batteries. *ACS Energy Lett.* **2018**, *3*, 992–996.

(19) Hartmann, P.; Leichtweiss, T.; Busche, M. R.; Schneider, M.; Reich, M.; Sann, J.; Adelhelm, P.; Janek, J. Degradation of NASICON-Type Materials in Contact with Lithium Metal: Formation of Mixed Conducting Interphases (MCI) on Solid Electrolytes. *J. Phys. Chem. C* **2013**, *117*, 21064–21074.

(20) Richards, W. D.; Miara, L. J.; Wang, Y.; Kim, J. C.; Ceder, G. Interface Stability in Solid-State Batteries. *Chem. Mater.* **2016**, *28*, 266–273.

(21) Zhu, Y.; He, X.; Mo, Y. Origin of Outstanding Stability in the Lithium Solid Electrolyte Materials: Insights from Thermodynamic Analyses Based on First-Principles Calculations. *ACS Appl. Mater. Interfaces* **2015**, *7*, 23685–23693.

(22) Zhu, Y.; He, X.; Mo, Y. First Principles Study on Electrochemical and Chemical Stability of the Solid Electrolyte-Electrode Interfaces in All-Solid-State Li-Ion Batteries. *J. Mater. Chem. A* **2015**, *4*, 3253–3266.

(23) Wenzel, S.; Weber, D. A.; Leichtweiss, T.; Busche, M. R.; Sann, J.; Janek, J. Interphase Formation and Degradation of Charge Transfer Kinetics between a Lithium Metal Anode and Highly Crystalline $Li_7P_3S_{11}$ Solid Electrolyte. *Solid State Ionics* **2016**, *286*, 24–33.

(24) Weber, D. A.; Senyshyn, A.; Weldert, K. S.; Wenzel, S.; Zhang, W.; Kaiser, R.; Berendts, S.; Janek, J.; Zeier, W. G. Structural Insights and 3D Diffusion Pathways within the Lithium Superionic Conductor $Li_{10}GeP_2S_{12}$. *Chem. Mater.* **2016**, *28*, 5905–5915.

(25) Takada, K. Solid State Lithium Battery with Oxysulfide Glass. *Solid State Ionics* **1996**, *86–88*, 877–882.

(26) Kitaura, H.; Hayashi, A.; Tadanaga, K.; Tatsumisago, M. High-Rate Performance of All-Solid-State Lithium Secondary Batteries Using $Li_4Ti_5O_{12}$ Electrode. *J. Power Sources* **2009**, *189*, 145–148.

(27) Kato, Y.; Hori, S.; Saito, T.; Suzuki, K.; Hirayama, M.; Mitsui, A.; Yonemura, M.; Iba, H.; Kanno, R. High-Power All-Solid-State Batteries Using Sulfide Superionic Conductors. *Nat. Energy* **2016**, *1*, 16030.

(28) Seino, Y.; Takada, K.; Kim, B.; Zhang, L.; Ohta, N.; Wada, H.; Osada, M.; Sasaki, T. Synthesis of Phosphorous Sulfide Solid Electrolyte and All-Solid-State Lithium Batteries with Graphite Electrode. *Solid State Ionics* **2005**, *176*, 2389–2393.

(29) Takada, K.; Inada, T.; Kajiyama, A.; Sasaki, H.; Kondo, S.; Watanabe, M.; Murayama, M.; Kanno, R. Solid-State Lithium Battery with Graphite Anode. *Solid State Ionics* **2003**, *158*, 269–274.

(30) Ohta, N.; Takada, K.; Sakaguchi, I.; Zhang, L.; Ma, R.; Fukuda, K.; Osada, M.; Sasaki, T. $LiNbO_3$-Coated $LiCoO_2$ as Cathode Material for All Solid-State Lithium Secondary Batteries. *Electrochem. Commun.* **2007**, *9*, 1486–1490.

(31) Ohta, N.; Takada, K.; Zhang, L.; Ma, R.; Osada, M.; Sasaki, T. Enhancement of the High-Rate Capability of Solid-State Lithium Batteries by Nanoscale Interfacial Modification. *Adv. Mater.* **2006**, *18*, 2226–2229.

(32) Han, F.; Zhu, Y.; He, X.; Mo, Y.; Wang, C. Electrochemical Stability of $Li_{10}GeP_2S_{12}$ and $Li_7La_3Zr_2O_{12}$ Solid Electrolytes. *Adv. Energy Mater.* **2016**, *6*, 1501590.

(33) Zhang, W.; Leichtweiß, T.; Culver, S. P.; Koerver, R.; Das, D.; Weber, D. A.; Zeier, W. G.; Janek, J. The Detrimental Effects of Carbon Additives in $Li_{10}GeP_2S_{12}$-Based Solid-State Batteries. *ACS Appl. Mater. Interfaces* **2017**, *9*, 35888–35896.

(34) Reimers, J.; Dahn, J. Electrochemical and In Situ X□Ray Diffraction Studies of Lithium Intercalation in Li_xCoO_2. *J. Electrochem. Soc.* **1992**, *139*, 2091–2097.

(35) Mizushima, K.; Goodenough, J. B.; Jones, P. C.; Wiseman, P. J. A New Cathode Material For Batteries Of High Energy Density. *Mat. Res. Bull.* **1980**, *15*, 783–789.

(36) Cho, J.; Kim, Y. J.; Kim, T. J.; Park, B. Zero-Strain Intercalation Cathode for Rechargeable Li-Ion Cell. *Angew. Chemie - Int. Ed.* **2001**, *40*, 3367–3369.

(37) Dokko, K.; Horikoshi, S.; Itoh, T.; Nishizawa, M.; Mohamedi, M.; Uchida, I. Microvoltammetry for Cathode Materials at Elevated Temperatures: Electrochemical Stability of Single Particles. *J. Power Sources* **2000**, *90*, 109–115.

(38) Wang, H.; Jang, Y.; Huang, B.; Sadoway, D. R.; Chiang, Y. TEM Study of Electrochemical Cycling-Induced Damage and Disorder in $LiCoO_2$ Cathodes for Rechargeable Lithium Batteries. *J. Electrochem. Soc.* **1999**, *146*, 473–480.

(39) McGrogan, F. P.; Swamy, T.; Bishop, S. R.; Eggleton, E.; Porz, L.; Chen, X.; Chiang, Y.-M.; Van Vliet, K. J. Compliant Yet Brittle Mechanical Behavior of Li_2S-P_2S_5 Lithium-Ion-Conducting Solid Electrolyte. *Adv. Energy Mater.* **2017**, *7*, 1602011.

(40) Sakuda, A.; Hayashi, A.; Tatsumisago, M. Interfacial Observation between $LiCoO_2$ Electrode and Li_2S-P_2S_5 Solid Electrolytes of All-Solid-State Lithium Secondary Batteries Using Transmission Electron Microscopy. *Chem. Mater.* **2010**, *22*, 949–956.

(41) Gong, Y.; Zhang, J.; Jiang, L.; Shi, J. A.; Zhang, Q.; Yang, Z.; Zou, D.; Wang, J.; Yu, X.; Xiao, R.; Hu, Y.-S.; Gu, L.; Li, H.; Chen, L. In Situ Atomic-Scale Observation of Electrochemical Delithiation Induced Structure Evolution of $LiCoO_2$ Cathode in a Working All-Solid-State Battery. *J. Am. Chem. Soc.* **2017**, *139*, 4274–4277.

(42) Wenzel, S.; Randau, S.; Leichtweiß, T.; Weber, D. A.; Sann, J.; Zeier, W. G.; Janek, J. Direct Observation of the Interfacial Instability of the Fast Ionic Conductor $Li_{10}GeP_2S_{12}$ at the Lithium Metal Anode. *Chem. Mater.* **2016**, *28*, 2400–2407.

(43) Gelius, U.; Hedén, P. F.; Hedman, J.; Lindberg, B. J.; Manne, R.; Nordberg, R.; Nordling, C.; Siegbahn, K. Molecular Spectroscopy by Means of ESCA. *Phys. Scr.* **1970**, *2*, 70–80.

(44) Abel, P. R.; Klavetter, K. C.; Jarvis, K.; Heller, A.; Mullins, C. B. Sub-Stoichiometric Germanium Sulfide Thin-Films as a High-Rate Lithium Storage Material. *J. Mater. Chem. A* **2014**, *2*, 19011–19018.

(45) Mitsa, V.; Holomb, R.; Kondrat, O.; Popovych, N.; Tsud, N.; Matolín, V.; Prince, K. C.; Lovas, G.; Petretskiy, S.; Tóth, S. Synchrotron XPS Studies of Illuminated and Annealed Flash Evaporated a-Ge_2S_3 Films. *J. Non. Cryst. Solids* **2014**, *401*, 258–262.

(46) Foix, D.; Martinez, H.; Gonbeau, D.; Granier, D.; Pradel, A.; Ribes, M. Thiogermanate Glasses-Influence of the Modifier Cation-a Combined XPS and Theoretical Study. *Phys. Chem. Chem. Phys.* **2005**, *7*, 180–186.

(47) Liang, X.; Hart, C.; Pang, Q.; Garsuch, A.; Weiss, T.; Nazar, L. F. A Highly Efficient Polysulfide Mediator for Lithium–sulfur Batteries. *Nat. Commun.* **2015**, *6*, 5682–5689.

(48) Aurbach, D.; Pollak, E.; Elazari, R.; Salitra, G.; Kelley, C. S.; Affinito, J. On the Surface Chemical Aspects of Very High Energy Density, Rechargeable Li–Sulfur Batteries. *J. Electrochem. Soc.* **2009**, *156*, A694–A702.

(49) Hakari, T.; Deguchi, M.; Mitsuhara, K.; Ohta, T.; Saito, K.; Orikasa, Y.; Uchimoto, Y.;

Kowada, Y.; Hayashi, A.; Tatsumisago, M. Structural and Electronic-State Changes of a Sulfide Solid Electrolyte during the Li Deinsertion–Insertion Processes. *Chem. Mater.* **2017**, *29*, 4768–4774.

(50) Sumita, M.; Tanaka, Y.; Ohno, T. Possible Polymerization of PS_4 at a Li_3PS_4 /$FePO_4$ Interface with Reduction of the $FePO_4$ Phase. *J. Phys. Chem. C* **2017**, *121*, 9698–9704.

(51) Auvergniot, J.; Cassel, A.; Foix, D.; Viallet, V.; Seznec, V.; Dedryvère, R. Redox Activity of Argyrodite Li_6PS_5Cl Electrolyte in All-Solid-State Li-Ion Battery : An XPS Study. *Solid State Ionics* **2017**, *300*, 78–85.

(52) Koerver, R.; Walther, F.; Aygün, I.; Sann, J.; Dietrich, C.; Zeier, W.; Janek, J. Redox-Active Cathode Interphases in Solid-State Batteries. *J. Mater. Chem. A* **2017**, *5*, 22750–22760.

(53) Dietrich, C.; Weber, D. A.; Culver, S.; Senyshyn, A.; Sedlmaier, S. J.; Indris, S.; Janek, J.; Zeier, W. G. Synthesis, Structural Characterization, and Lithium Ion Conductivity of the Lithium Thiophosphate $Li_2P_2S_6$. *Inorg. Chem.* **2017**, *56*, 6681–6687.

(54) Oh, G.; Hirayama, M.; Kwon, O.; Suzuki, K.; Kanno, R. Bulk-Type All Solid-State Batteries with 5 V Class $LiNi_{0.5}Mn_{1.5}O_4$ Cathode and $Li_{10}GeP_2S_{12}$ Solid Electrolyte. *Chem. Mater.* **2016**, *28*, 2634–2640.

For Table of Contents only